Improving Estimation of Specific Differential Phase and Assessing Differential Backscattering Phase

REESE MISHLER,[a,b] GUIFU ZHANG,[a,b] AND VIVEK N. MAHALE[c]

[a] *School of Meteorology, University of Oklahoma, Norman, Oklahoma*
[b] *Advanced Radar Research Center, Norman, Oklahoma*
[c] *NOAA/National Weather Service, Norman, Oklahoma*

(Manuscript received 24 October 2023, in final form 11 April 2024, accepted 3 May 2024)

ABSTRACT: Polarimetric variables such as differential phase Φ_{DP} and its range derivative, specific differential phase K_{DP}, contain useful information for improving quantitative precipitation estimation (QPE) and microphysics retrieval. However, the usefulness of the current operationally utilized estimation method of K_{DP} is limited by measurement error and artifacts resulting from the differential backscattering phase δ. The contribution of δ can significantly influence the Φ_{DP} measurements and therefore negatively affect the K_{DP} estimates. Neglecting the presence of δ within non-Rayleigh scattering regimes has also led to the adoption of incorrect terminology regarding signatures seen within current operational K_{DP} estimates implying associated regions of unrealistic liquid water content. A new processing method is proposed and developed to estimate both K_{DP} and δ using classification and linear programming (LP) to reduce bias in K_{DP} estimates caused by the δ component. It is shown that by applying the LP technique specifically to the rain regions of Rayleigh scattering along a radial profile, accurate estimates of differential propagation phase, specific differential phase, and differential backscattering phase can be retrieved within regions of both Rayleigh and non-Rayleigh scattering. This new estimation method is applied to cases of reported hail and tornado debris, and the LP results are compared to the operationally utilized least squares fit (LSF) estimates. The results show the potential use of the differential backscattering phase signature in the detection of hail and tornado debris.

KEYWORDS: Hail; Radars/Radar observations; Weather radar signal processing; Optimization

1. Introduction

The upgrade to dual polarization on weather radar networks such as the U.S. National Weather Service (NWS) Weather Surveillance Radar-1988 Doppler (WSR-88D) has allowed for new insight and understanding into cloud microphysics and advanced severe weather applications such as hail and tornado detection. The inclusion of the total differential phase Φ_{DP} and its range derivative, specific differential phase K_{DP}, has helped improve hydrological applications, such as quantitative precipitation estimation (QPE) (Brandes et al. 2002; Ryzhkov et al. 2005a; Huang et al. 2016). The term K_{DP} has shown immunity to radar miscalibration, partial beam blockage, and precipitation attenuation. It is also less sensitive to hail contamination and variability in the raindrop size distribution (DSD). Therefore, K_{DP} is more favorable for obtaining accurate precipitation estimation and microphysical retrievals than reflectivity measurements (Aydin et al. 1995; Zrnić and Ryzhkov 1996; Bringi and Chandrasekar 2001; Ryzhkov et al. 2005a; Wang and Chandrasekar 2010; Giangrande et al. 2013; Huang et al. 2016; Ralph-Hampton 2022).

However, despite these advantages, acquiring accurate estimates of K_{DP} ($\hat{K}_{DP}$) from Φ_{DP} measurements has been a challenge. Uncertainty in $\hat{K}_{DP}$ can result in detrimental effects on rain estimation. As shown in Eq. (4.144) of Zhang (2016), the total differential phase from the phase of the copolar cross-correlation function is $\Phi_{DP} = \phi_{DP} + \delta$ where ϕ_{DP} is the differential propagation phase and δ is the differential backscattering phase. Therefore, the total Φ_{DP} measurement ($\hat{\Phi}_{DP}$) is the sum of Φ_{DP} and measurement error ε, yielding $\hat{\Phi}_{DP} = \Phi_{DP} + \varepsilon = \phi_{DP} + \delta + \varepsilon$ (Doviak and Zrnić 1993; Bringi and Chandrasekar 2001; Trömel et al. 2013; Kumjian 2013; Ralph-Hampton 2022). Falling hydrometeors are typically oriented with their larger axis parallel to the ground. As a result, a horizontally polarized wave has a greater interaction with the hydrometeor than a vertically polarized wave, yielding a larger propagation constant (or wavenumber) for horizontal polarization than that for vertical polarization in rain when the Rayleigh scattering approximation is valid (Doviak and Zrnić 1993; Bringi and Chandrasekar 2001; Westbrook et al. 2010; Ralph-Hampton 2022). Thus, it is expected that intrinsic K_{DP} is positive and ϕ_{DP} is monotonically increasing along the beam within rain at S band frequency (Vivekanandan et al. 2001; Brandes et al. 2002). However, these expected properties for K_{DP} and ϕ_{DP} at S band are not true for other hydrometeors such as hail, melting snow, and tornado debris due to the effects of non-Rayleigh scattering as illustrated in Fig. 1, shown in next section.

While K_{DP} is normally understood and physically defined as the range derivative of the differential propagation phase ϕ_{DP} with $K_{DP} = (1/2)(d\phi_{DP}/dr)$, where r is the distance from radar of a given range gate, it is usually estimated as the range derivative of $\hat{\Phi}_{DP}$ ($d\hat{\Phi}_{DP}/dr$) using the least squares fit (LSF), which can be misleading. Measurement error ε can often be minimized via LSF and other smoothing techniques or treated as negligible. However, the contribution of the differential backscattering phase δ can significantly influence the $\hat{\Phi}_{DP}$ and

Corresponding author: Reese Mishler, reese.mishler@ou.edu

DOI: 10.1175/JAMC-D-23-0204.1

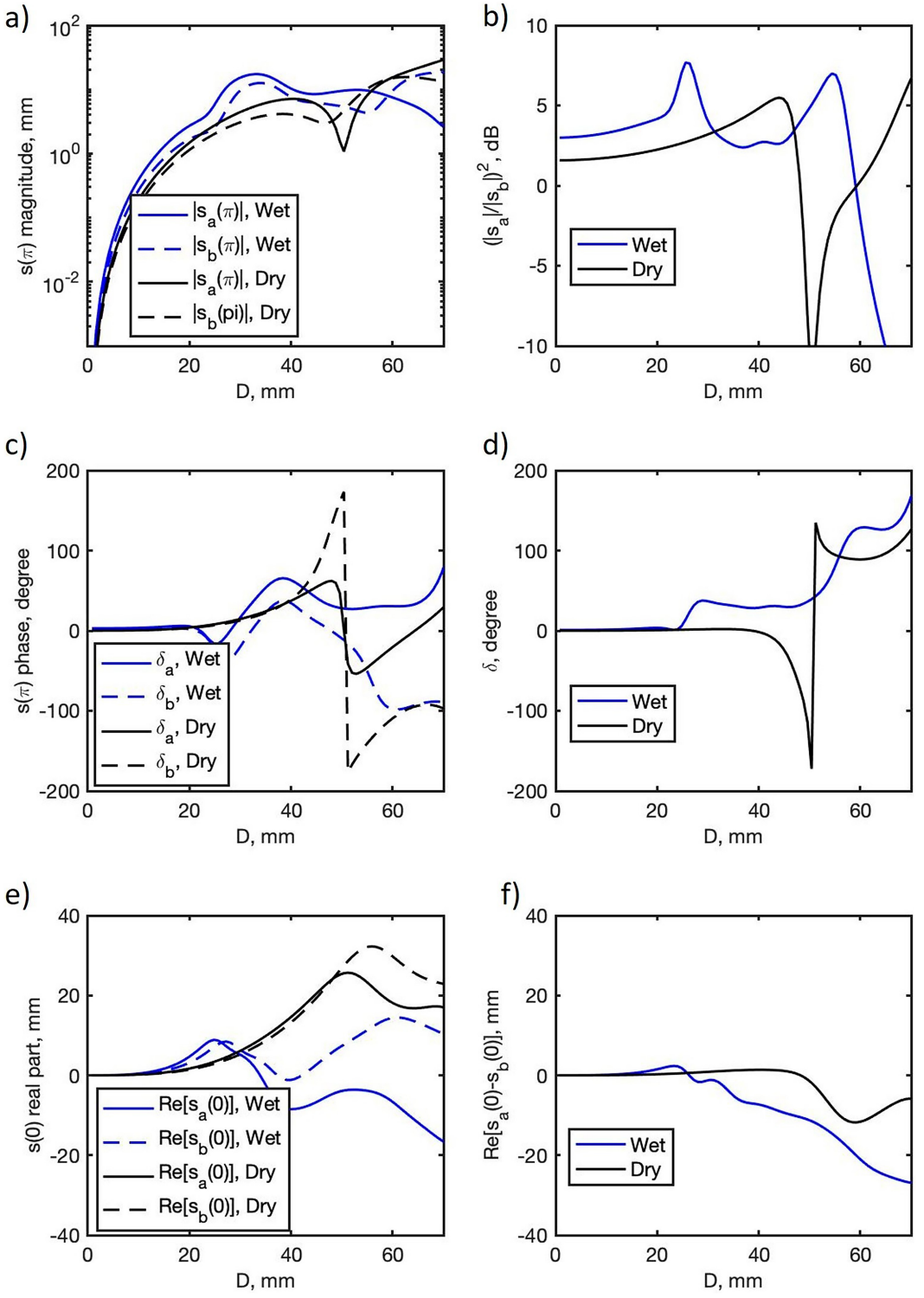

FIG. 1. Scattering calculations using the T-matrix method for both wet (blue) and dry (black) hail: (a) absolute value of backscattering magnitude as a function of diameter for both horizontal (solid) and vertical (dashed) axis, (b) squared ratio of horizontal and vertical absolute scattering magnitude, (c) backscattering phase for both horizontal and vertical axes, (d) differential backscattering phase ($\delta_a - \delta_b$), (e) real parts of forward scattering amplitudes for horizontal and vertical axes, and (f) difference in real parts of the forward scattering amplitudes.

therefore negatively affect the K_{DP} estimation, which can then propagate through all products derived using $\hat{K}_{DP}$ (Trömel et al. 2013; Ralph-Hampton 2022). This is particularly true for hail and tornado debris which scatter waves in non-Rayleigh scattering regimes. Ignoring the contributions of δ when estimating K_{DP} from $\hat{\Phi}_{DP}$ can often result in unphysical behavior such as unrealistically large $\hat{K}_{DP}$ and negative $\hat{K}_{DP}$ with corresponding unreasonable rainfall rates on leading and trailing sides of hail and/or the melting layer (Giangrande and Ryzhkov 2008). Furthermore, ignoring the presence of δ has led to an adoption of incorrect terminology regarding signatures seen within the current operational usage of K_{DP} estimates.

The term "KDP foot" has been used to explain an area within a supercell containing enhanced $\hat{K}_{DP}$ (sometimes $>8°$ km^{-1}) which can be found when using LSF processing as implemented by the WSR-88D network. This KDP foot is used as an indicator for hail, particularly at the leading edge of the KDP foot signature (Romine et al. 2008; Wilson and Van Den Broeke 2021). The terminology used to describe this signature suggests a general misunderstanding with K_{DP}, which leads to further misinterpretation regarding the physical nature of the region such that the KDP foot signature is associated with enhanced liquid water content (Wilson and Van Den Broeke 2021). Though large intrinsic K_{DP} within pure rain regimes is indicative of high liquid water content, we cannot extend this association into non-Rayleigh scattering regimes using the conventionally estimated $\hat{K}_{DP}$. It is unlikely to be true that such high liquid water content, associated with the LSF estimated KDP foot signature, should be possible to exist. Given that the presence of hail is often associated with the estimated KDP foot region, it is likely that the addition of significant δ is largely contributing to this signature. Hence, using the term KDP foot to define the region is erroneous because it is not only the result of true K_{DP} but also of the additional artifact from δ. The artifact can be a dominant factor, especially for melting hail.

These issues highlight the necessity for processing techniques that separate the δ from the ϕ_{DP} such that K_{DP} can be accurately estimated, and precipitation microphysics may be ascertained from these components correctly. A more accurate K_{DP} estimate will lead to a more accurate precipitation estimation. Furthermore, research has shown that δ shows promise for not only locating scatterers such as hail and tornado debris but also allowing for insight into the size of these scatterers when it is used together with other polarimetric radar variables such as the copolar correlation coefficient ρ_{hv} (Zhang 2016; Zhang et al. 2021).

Though many methods have been proposed for handling the aforementioned challenge (Ryzhkov et al. 2005a; Wang and Chandrasekar 2009; Otto and Russchenberg 2011), linear programming (linear optimization) has been shown to effectively avoid the δ component, thus maintaining a monotonic increase of ϕ_{DP} and nonnegative, unbiased K_{DP} profiles within rain regimes (Giangrande et al. 2013; Huang et al. 2016). Though this method is computationally expensive, the rapid increases in computing power have made it a more viable option in recent years. Using the $\hat{\Phi}_{DP}$ and a series of linear constraints, this method can back out a ϕ_{DP} profile that has an optimally minimized difference from the given $\hat{\Phi}_{DP}$ profile per the provided constraints. It has been assessed by Giangrande et al. (2013) that the mean bias error for LP estimation of K_{DP} is about 0.1° km^{-1}, which is smaller than that of 0.18° km^{-1} for LSF estimation. Due to the linear programming (LP) method's proven success within rain regimes, it is reasonable to assume that the LP method can be used specifically within regimes of Rayleigh scattering to produce realistic estimates for radial profiles of both ϕ_{DP} and K_{DP}. Furthermore, by applying the technique specifically to Rayleigh scattering regimes along a radial profile, an estimate of δ can be retrieved within non-Rayleigh scattering regimes.

The remainder of this article is structured as follows. Section 2 provides background information on wave propagation and scattering and explores some past research that has been done to estimate K_{DP} while minimizing the influence of non-Rayleigh scattering regimes. Section 3 details the methodology of applying the LP technique within Rayleigh scattering regimes to obtain 2D estimated profiles of ϕ_{DP}, K_{DP}, and δ. Section 4 presents the estimation results obtained from applying this method to some collected NEXRAD Level II datasets (S band) and expands on the findings of detection. The results are further summarized and concluded in section 5.

2. Background

As we seek to better understand the estimation and utilization of K_{DP} and δ, it is desirable to examine both within a theoretical framework. The plots in Fig. 1 were created using the T-matrix calculation method (Waterman 1965; Vivekanandan et al. 1991) to illustrate the backscattering magnitude, backscattering phase, and real parts of the forward scattering amplitude. Results for polarizations at both the major and minor axes are shown for both wet and dry hailstones as a function of the equivolume diameter. The hailstones were assumed to be oblate spheroids with an axis ratio of 0.7. For the wet hail, the dielectric constant was calculated using the Maxwell–Garnett (M–G) mixing formula with the assumption of 20% melting and water as background following the melting model used in Jung et al. (2008) and Zhang et al. (2021). Figure 1a illustrates the absolute value of the scattering amplitude. The square of this is proportional to the scattering cross section and thus proportional to the radar reflectivity factor (Z_H or Z_V). Initially, we do see a monotonic increase in this scattering amplitude which follows Rayleigh scattering. However, once the size of the hydrometeor surpasses the Rayleigh scattering size, we begin to see resonance effects. Figure 1b shows the squared absolute value of the ratio in scattering amplitude between the major and minor axis polarizations. This is the differential reflectivity Z_{DR} for monodispersive hailstones. With the aforementioned assumptions, we initially see values increase and remain greater than zero. The Z_{DR} for the "wet" spheroid continues to increase until a maximum is reached near ~25 mm before decreasing. The Z_{DR} for the "dry" spheroid also increases until a maximum is reached, though this occurs at a larger diameter (~42 mm) due to the lower dielectric constant. For both "wet" and "dry," resonance effects begin to set in after the maximum is reached after which negative values may occur. The behavior displayed by the "dry" hail illustrated in Fig. 1b closely

resembles the results shown by Seliga and Bringi (1978). These kinds of resonance effects are also seen in polarimetric radar data of tornado debris, which will be discussed in section 4.

Figure 1c shows the phase of the scattered waves polarized in the major and minor axes for both wet and dry hail. Initially, phase increases for both. At approximately 19 mm, we begin to see a decrease in phase for both axes of the wet particle though this decrease is short lived and followed by a significant increase from ~22 to 39 mm. The dry particle maintains its increase in the phase for both axes up until ~50 mm where both show a sharp decrease though the abrupt change for δ_b is due to phase folding. Somewhere after ~50 mm, each axis of both the wet and dry particles again shows some magnitude of the increased phase. In Fig. 1d, we take the difference of the backscattering phases in both polarizations, which corresponds to the differential backscattering phase δ. Using the T-matrix calculation with an aspect ratio of 0.8, Balakrishnan and Zrnić (1990) showed that spongy hail (40% water) could produce substantial variations in delta beyond 5 cm displaying values between −50° and 90°, while dry hail showed very little δ (only ~8° at 8 mm and falling to −20° at 50 mm). Our calculations yielded similar trends but different values because a different implementation of the M–G mixing formula, aspect ratio (0.7), and percentage of melting (20%) were used. Apart from hailstones with a small diameter (<10 mm), this δ is nonnegligible. Though dry hail (or low melting percentage hail) showed near constant values near zero until 50 mm, we then see that δ can rapidly become negative. Our wet hail calculation shows that δ tends to increase with size. Slight increases are seen up to ~20 mm (~10°) before jumping to ~40° by 27 mm and again to ~125° at 55 mm.

In Fig. 1e, we plot the real parts of the forward scattering for both the major and minor axes. These are related to the specific propagation phase due to the presence of hydrometeors. The specific differential phase is expressed by Eq. (4.106) of Zhang (2016):

$$K_{\mathrm{DP}} \approx \frac{180\lambda}{\pi}\int \mathrm{Re}[s_a(0, D) - s_b(0, D)]N(D)dD\frac{1}{2}(1 + e^{-2\sigma_\vartheta^2})e^{-2\sigma_\varphi^2},$$

as the integration of the difference between the real parts of the forward scattering amplitudes (s_a and s_b) at the major and minor axes weighted by DSD and canting angle parameters where σ_ϑ and σ_φ are the standard deviation of canting angles in the scattering plane and the polarization plane. As shown in Fig. 1f, initially, we do see an increase in the difference. After the "wet" hail grows beyond ~25 mm in diameter, negative values begin to occur. The dry hail shows a larger range of positive values, with negative values not reached until a diameter of ~50 mm. This suggests that even well-defined K_{DP} does not behave as a monotonic function outside of the Rayleigh scattering regime. This helps illustrate why, particularly in the operational processing of $\hat{K}_{\mathrm{DP}}$, simple explanations for negative values (i.e., vertically oriented particles due to charge differentials in elevation) may not always be correct. Different scenarios might result in this negative K_{DP}, each with different physics, in addition to those caused by δ and measurement error ε, mentioned earlier. The occurrence of nonuniform beamfilling can also result in negative K_{DP}, particularly along the melting layer (Ryzhkov and Zrnić 1998). Along with vertically aligned ice particles within Rayleigh scattering regimes, we may also see estimation error causing a "bump" in $\hat{\Phi}_{\mathrm{DP}}$. The LSF processing will result in negative values of $\hat{K}_{\mathrm{DP}}$ along the trailing end of the said bump. Figure 1f shows negative K_{DP} may also arise from large particles outside of the Rayleigh scattering regime.

From the definition of $K_{\mathrm{DP}} = (1/2)(d\phi_{\mathrm{DP}}/dr)$, the specific differential phase can be estimated from two measurements of Φ_{DP} at two consecutive range gates as follows:

$$\hat{K}_{\mathrm{DP}} = \frac{1}{2}\frac{\hat{\Phi}_{\mathrm{DPDP}}(r_2) - \hat{\Phi}_{\mathrm{DP}}(r_1)}{(r_2 - r_1)}, \tag{1}$$

when $\hat{\Phi}_{\mathrm{DP}}$ contains no differential backscattering phase δ and is devoid of ε. Given that the statistical error can often be prevalent, acquiring a valid $\hat{K}_{\mathrm{DP}}$ result per Eq. (1) is impractical. Due to the relative consistency in hydrometeor characteristics from one gate to the next, estimations are often made using more than two gates to solve this issue, but in using multiple measurements, the estimation of K_{DP} can become overdetermined (Rodgers 2000). The simple regression method of LSF is the operationally used approach for acquiring solutions to the overdetermined system. This approach uses the LSF slope of multiple $\hat{\Phi}_{\mathrm{DP}}$ measurements adjacent to the range gate at which a K_{DP} estimate is sought. The WSR-88D systems use a piecewise approach to determine the filter lengths (i.e., 9 or 25 gates, which is equivalent to the range resolution of 2.25 or 6.25 km) contingent on the reflectivity Z_{H} at a given gate. When the Z_{H} is at or below 40 dBZ for an intermediate gate, a filter length of 25 gates is used to make the estimation. When the Z_{H} exceeds 40 dBZ, the filter length is reduced to 9 measurements surrounding the intermediate gate. Thus, the LSF estimation method can be calculated as follows (Doviak and Zrnić 1993):

$$\hat{K}_{\mathrm{DP}}(\bar{r}) = \frac{\sum_{i=1}^{n}\left\{\left[\hat{\Phi}_{\mathrm{DP}}(i) - \overline{\hat{\Phi}}_{\mathrm{DP}}\right][r(i) - \bar{r}]\right\}}{2\sum_{i=1}^{n}[r(i) - \bar{r}]^2}. \tag{2}$$

Here, $\hat{K}_{\mathrm{DP}}(\bar{r})$ is the estimated value at the mean range, which is the distance of the intermediate gate, n is the filter length (either 9 or 25 gates), and $\hat{\Phi}_{\mathrm{DP}}$ is the mean value across the filter length. This estimation technique can mitigate ε in the measurements, but it still includes artifacts from the δ inherent within some Φ_{DP} measurements. There have been some advancements in the estimation of K_{DP} by trying to mitigate the effect of non-Rayleigh scattering regimes. Giangrande et al. (2013) presented an application of LP to $\hat{\Phi}_{\mathrm{DP}}$ with the aim of estimating the differential propagation phase ϕ_{DP} with monotonic profiles and nonnegative constraints applied to the $\hat{K}_{\mathrm{DP}}$ retrieval. Huang et al. (2016) expanded upon this methodology by setting upper and lower limits to the K_{DP} estimation determined by a constraint among Z_{H}, Z_{DR}, and $\hat{\Phi}_{\mathrm{DP}}$ measurements. These limits are then incorporated into the LP system. However,

even with these advancements, there have yet to be successful attempts at estimating and utilizing δ.

The methodology used in this study is a composite approach combining classification techniques and fitting techniques such that the fitting is only performed within certain classifications. It will build upon previous research by using the LP approach across identified intervals of Rayleigh scattering along a given radial. Each gate will be classified as either a Rayleigh or non-Rayleigh scattering regime using the measurements of Φ_{DP}, Z_H, and ρ_{hv}. This should allow for accurate estimates of ϕ_{DP} and K_{DP} to be obtained within Rayleigh regimes such that we may interpolate these measurements in adjacent non-Rayleigh scattering regimes and then obtain estimates of δ.

3. Methodology

This section will provide a detailed description of how the estimation of ϕ_{DP}, K_{DP}, and δ is performed. Briefly, the procedure can be broken down into the following steps: segments of Rayleigh scattering are identified and separated from non-Rayleigh scattering regimes. An estimation of ϕ_{DP} and K_{DP} is performed for each Rayleigh scattering segment using linear programming. Along a given radial, these Rayleigh scattering segments are connected to provide an estimation of ϕ_{DP} and K_{DP} within non-Rayleigh scattering regimes. The ϕ_{DP} and K_{DP} estimation results are then smoothed for display purposes. Finally, δ is estimated from the difference between the $\hat{\Phi}_{DP}$ and the estimated ϕ_{DP}. These steps are illustrated within the flow diagram depicted in Fig. 2. We will now provide more detail of each of these steps within the estimation process.

The estimation process begins by calculating a starting ϕ_{DP} value to be used for each radial as shown in Fig. 2a. For each radial, the first 15 range gates are inspected. Any gate that has ρ_{hv} less than 0.96 or both Z_H less than 0 dBZ and signal-to-noise ratio (SNR) less than 20 dB will be omitted. The median value is then taken from the remaining gates. This is done for each azimuth angle such that each angle provides one median value. From the values returned across all azimuth angles, a median is taken to determine the starting ϕ_{DP} value. This starting value will be used as the initial lower bound constraint for the linear programming function and will also be applied to all gates prior to the first Rayleigh scattering regime for each radial.

Since theory necessitates ϕ_{DP} be estimated within Rayleigh scattering regimes, it is necessary to locate the gates at which those regimes might exist before the actual estimation process commences. This step is illustrated by the flow diagram in Fig. 2b. To do this, a 5-point sliding window is used to move down a given radial while analyzing the measured Z_H, Z_{DR}, ρ_{hv}, and Φ_{DP}. Because of potential clutter contamination of near-radar gates, stricter conditions are established for the first 11 km. In this zone, each gate within a 5-point window must contain ρ_{hv} greater than 0.96, SNR larger than 20 dB, and Z_H larger than 0 dBZ for the gates within the window to be considered as Rayleigh regime gates. Furthermore, to ensure low variability among the Φ_{DP} measurements in the window, the standard deviation of $\hat{\Phi}_{DP}$ across the five gates must be no higher than 6°. If each

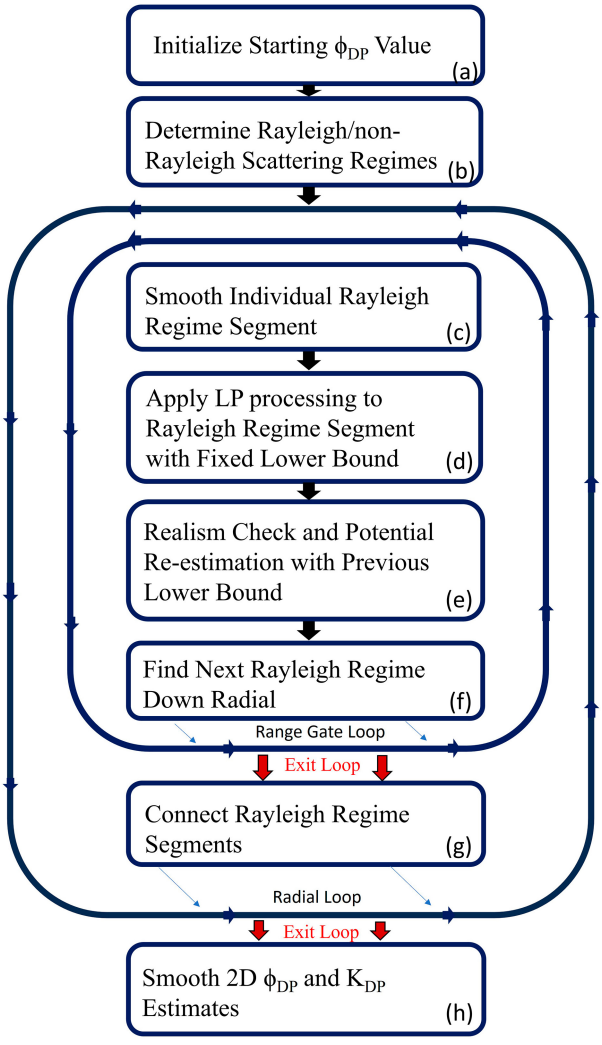

FIG. 2. A flow diagram illustrating the process used for estimating the differential propagation phase ϕ_{DP} and specific differential phase K_{DP} at a given elevation of a NEXRAD Level II data file. The range gate loop indicates traversing down range of a given radial, while the radial loop indicates looping over radials at all azimuth angles.

of these conditions is met, we flag these gates as being "good" (i.e., gates determined to be Rayleigh scattering regime). Past 11 km, nearly the same restrictions are applied with the differences being that the ρ_{hv} threshold is reduced to 0.95, the SNR threshold is reduced to 5 dB, and a single gate within the 5-point window may deviate from the restrictions (i.e., a single gate may have either a ρ_{hv}, SNR, or Z_H value below the given thresholds). The combination of thresholds was chosen based on our physical understanding of Rayliegh scattering regimes and their ability to return reasonable results.

We begin the estimation process by finding the first Rayleigh gate in a given radial using the flags created. We begin looping from this point to the end of the 1D radial vector (illustrated by the inner loop in Fig. 2). If we encounter a "bad" (non-Rayleigh) gate, the window automatically closes. If we encounter a NaN

value in the measured $\hat{\Phi}_{DP}$, we mark this position and then look forward to the next good gate while tracking the number of consecutive NaN values that occur before this location. In the case that either a "bad" gate was encountered, or 3+ consecutive NaN values were encountered, the estimate window is fixed from the starting position of the window up to the gate prior to the consecutive NaNs or non-Rayleigh regime gate. Due to the possibility that a NaN value could exist within this estimation window, a 3-point median filter is applied to the window to ensure no NaN values exist within the estimate window as depicted in Fig. 2c of the flowchart. At this point, a LP estimation of both ϕ_{DP} and K_{DP} will be performed on the segment vector (Fig. 2d). The methodology outlined in Giangrande et al. (2013) is utilized such that, through a series of linear constraints, an optimally minimized difference between the provided $\hat{\Phi}_{DP}$ profile and the corresponding ϕ_{DP} can be achieved, while the monotonic constraint will also allow for the return of a nonnegative profile of K_{DP}.

By instantiating a monotonic increase constraint along each radial, the last value of the estimated ϕ_{DP} window will be set as the lower bound for the next window estimated down radial. The next estimate will begin from the next good gate following the previous estimation window as depicted in Fig. 2f. There is a possibility that, even with the thresholds set to establish a good Rayleigh scattering gate, the classification could have been faulty. Thus, measures have been established to counteract the possibility that an estimate window results in an unrealistically high lower bound that skews the results of the rest of the down-radial segments as illustrated in Fig. 3. This is done by analyzing the difference between the $\hat{\Phi}_{DP}$ at the first gate of a new estimation window and the current lower bound (estimated propagation phase of final gate in previously estimated window).

Figure 3a depicts a faulty estimate segment (circled in black) at ~47 km. The estimated ϕ_{DP} for the last gate of this segment is then set to be used as the lower bound for the next Rayleigh scattering segment (boxed in red) at ~50 km. This lower bound is nearly 40° higher than the $\hat{\phi}_{DP}$ recorded at the range the final Rayleigh regime begins. As shown in Fig. 3a, were we to allow this lower bound to be used in the LP estimation, the monotonic increase constraint would result in an unrealistically large estimate. In this case, the previous estimate (circled in black in Fig. 3a) is omitted. The final segment is instead estimated using the lower bound given by the previous Rayleigh up-radial segment. This is illustrated in Fig. 3b, where the lower bound provided by the upstream Rayleigh estimate at ~30 km (circled in black) is used for the final segment (boxed in red). This results in a much more realistic estimate for the down-radial segment with the faulty region now being classified as non-Rayleigh and thus no longer containing an estimate.

After these steps have been completed for the entire radial, we move on to connecting the Rayleigh regimes as shown in Fig. 2g. First, all values in the estimate vector prior to the first Rayleigh regime gate are set to the starting point value. The final index of the first Rayleigh regime segment is marked as the left bookend, and the first index of the second Rayleigh regime segment is set as the right bookend. A linear interpolation is done between these two bookends to estimate the

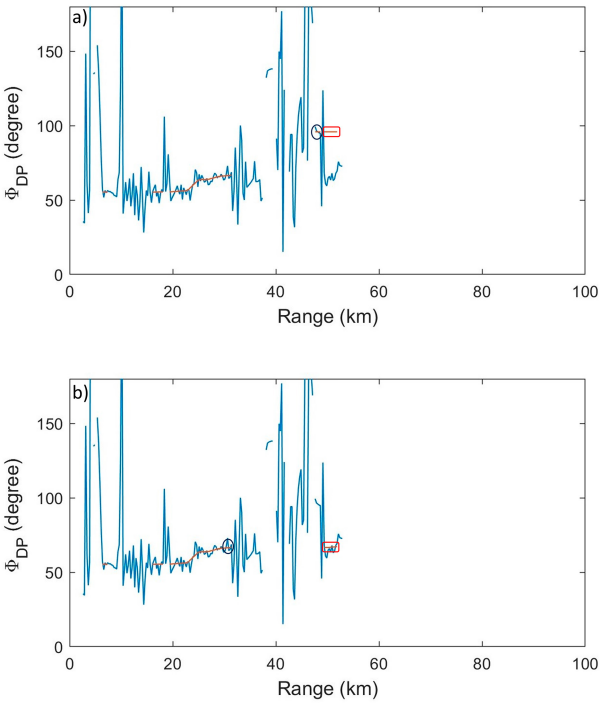

FIG. 3. (a) How an incorrectly classified Rayleigh scattering estimate (circled) can result in a lower bound that causes a down-radial estimation (boxed in red) to be unrealistically high. (b) The same radial estimation of ϕ_{DP} with the faulty segment removed such that the later segment (boxed in red) would have been estimated with the lower bound provided by the previously estimated, up-radial segment (circled in black).

ϕ_{DP} and K_{DP} along the non-Rayleigh scattering regime. This process of connecting bookends continues down the rest of the radial. Any non-Rayleigh scattering gate past the final Rayleigh scattering segment is set to NaN within the ϕ_{DP} estimate vector. Figure 4 illustrates the results of this step for a single ray. Figure 4a shows a radial in which an LP estimation of ϕ_{DP} has been made for each Rayleigh scattering segment. Figure 4b shows how a linear interpolation can be done between these Rayleigh scattering segments to estimate the ϕ_{DP} in the non-Rayleigh scattering regimes.

After the connection process has been completed for each radial, smoothing is performed for display purposes for both estimates depicted in Fig. 2h. A 3-point median filter is applied azimuthally to the K_{DP} estimate for smoothing between radials. Within the ϕ_{DP} estimate, each gate with a NaN value is checked to see if its adjacent gates of the same range have non-NaN estimates. Linear interpolation is used to estimate these NaN values, and a moving average is applied azimuthally to smooth between radials using a 3-point sliding window. With the estimates of ϕ_{DP} and K_{DP} now complete, the differential backscattering phase δ is estimated simply by taking the difference between the $\hat{\Phi}_{DP}$ and the estimated ϕ_{DP}.

We acknowledge that within the non-Rayleigh scattering regions, the linear interpolation estimate of the ϕ_{DP} (which could differ slightly from the true propagation phase) may

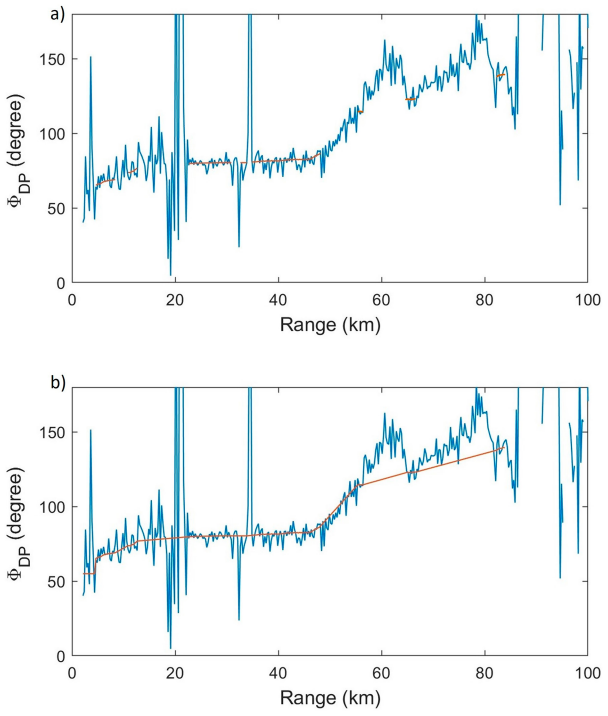

FIG. 4. (a) The $\hat{\Phi}_{DP}$ (blue) and the unconnected estimated ϕ_{DP} within the determined Rayleigh scattering regimes (red). (b) As in (a), but with linear interpolation used to connect the Rayleigh scattering regimes providing an estimation of ϕ_{DP} in non-Rayleigh scattering regimes.

negatively affect the estimation of the δ. Furthermore, the estimated δ likely contains some components from the measurement errors. However, we believe this effect would be relatively small as a differential backscattering phase tends to be on the order of 10°, which should allow the estimation made through the simple connection to be within a few degrees. The "fixed" value of K_{DP} made throughout the non-Rayleigh scattering regime would also likely differ from the true K_{DP} in this region, which would show more variation. The intrinsic K_{DP} along the non-Rayleigh regime is dependent upon several unknowns (size, shape, composition, percentage of melting, etc.). Because there is not yet a community-accepted way of accurately determining these parameters, we chose the linear interpolation for K_{DP} estimation in non-Rayleigh scattering regimes, which may be improved with further study.

4. Results

The methodology detailed above was applied to a case from 19 April 2023, when there was a 7.6-cm (3 in.) diameter hailstone reported in Amber, Oklahoma (SPC 2023). We are using the level-II data at the low elevation (0.5°) collected by the WSR-88D KTLX (Oklahoma City, Oklahoma) system at 2330 UTC. These files were obtained from Amazon Web Services (AWS 2023). Furthermore, we will briefly analyze two tornado events in which discernable δ signatures were collocated with tornado debris signatures (TDSs; Ryzhkov et al. 2005b; Kumjian and Ryzhkov 2008). Specifically, we will analyze the signature from the EF4 tornado that devastated Rolling Fork, Mississippi, on 24 April 2023 and the EF3 tornado that hit Cole, Oklahoma, on 31 March 2023.

Figure 5 illustrates the supercell that produced the 7.6-cm (3 in.) hailstone as it moved into Amber, Oklahoma, just minutes before the time of the reports. We see the well-defined reflectivity Z_H signature of the supercell in Fig. 5a to the southwest of the KTLX. At the center of the supercell, we see reflectivity values that exceed 60 dBZ indicating the likely presence of hail (region circled in black). Figure 1b illustrates how differential reflectivity Z_{DR} can become negative when hailstones grow beyond the Rayleigh scattering regime, and in Fig. 5b, we see Z_{DR} values fall below 0 dB in the area of elevated Z_H values. Furthermore, Fig. 5c shows that ρ_{hv} values fall below 0.9 in this region. This drop in ρ_{hv}, along with the Z_H and Z_{DR} signatures, provides a compelling case for the presence of hail. Figure 5d depicts a large increase in the total differential phase measurements $\hat{\Phi}_{DP}$ near the vicinity of this hail core. Downrange of the well-defined supercell (west-southwest) is another region of enhanced reflectivity (boxed in black). This region also seems to show indications of a hail signature with near-zero Z_{DR} values, low ρ_{hv} values (<0.9), and Z_H values greater than 55 dBZ.

We have selected a single 1D ray to analyze from the scan which, in each plot of Fig. 5, is shown as the black ray emanating from the radar. This ray passes through the north-northeastern periphery of both hail signatures. As per Fig. 1d, resonance effects begin after the dry hailstone grows beyond ~40 mm, so we chose a ray passing along the peripheries of the hail cores in order to best illustrate positive δ. The 1D plots associated with this ray can be seen in Fig. 6. From ~49 to 60 km, we see the Z_H values above 50 dBZ as seen between the orange dashed lines in Fig. 6c. We also see Z_{DR} values begin to drop from ~5 dB at ~50 km and hit a local minimum of ~−0.5 dB at ~57 km which is consistent with resonance effects we saw in Fig. 1b. The $\hat{\Phi}_{DP}$ remains relatively constant until ~50 km where it then begins increasing. However, at ~56 km, we see the $\hat{\Phi}_{DP}$ slope begin to increase more rapidly hitting a local maximum in magnitude of measured values at ~60 km. The $\hat{\Phi}_{DP}$ then begins to fall until ~65 km. The local maximum in $\hat{\Phi}_{DP}$ associated with this bump appears slightly downrange of the highest Z_H values, which agrees with the plots in Fig. 1 that demonstrate how the maximum reflectivity does not necessarily correspond with the maximum backscattering phase. However, the bump does occur within the apparent hail signature per the trends in ρ_{hv} and Z_{DR}. We see a very similar trend downrange near ~75–80 km corresponding to the second enhanced reflectivity regime (between the vertical black dashed lines). Again, the local $\hat{\Phi}_{DP}$ maximum is slightly down radial of the local Z_H maximum though still in phase with low values of ρ_{hv} and Z_{DR}. These results suggest that these bumps in $\hat{\Phi}_{DP}$ are likely due to the differential backscattering phase from hailstones exceeding the size of the Rayleigh scattering regime. It is possible that the effects of differential attenuation and nonuniform beamfilling might be contributing to these low values ρ_{hv} and Z_{DR}, particularly where we see the second peak in $\hat{\Phi}_{DP}$ which is collocated with Z_H values of ~30 dBZ. Here, we are analyzing beams that pass just along reflectivity

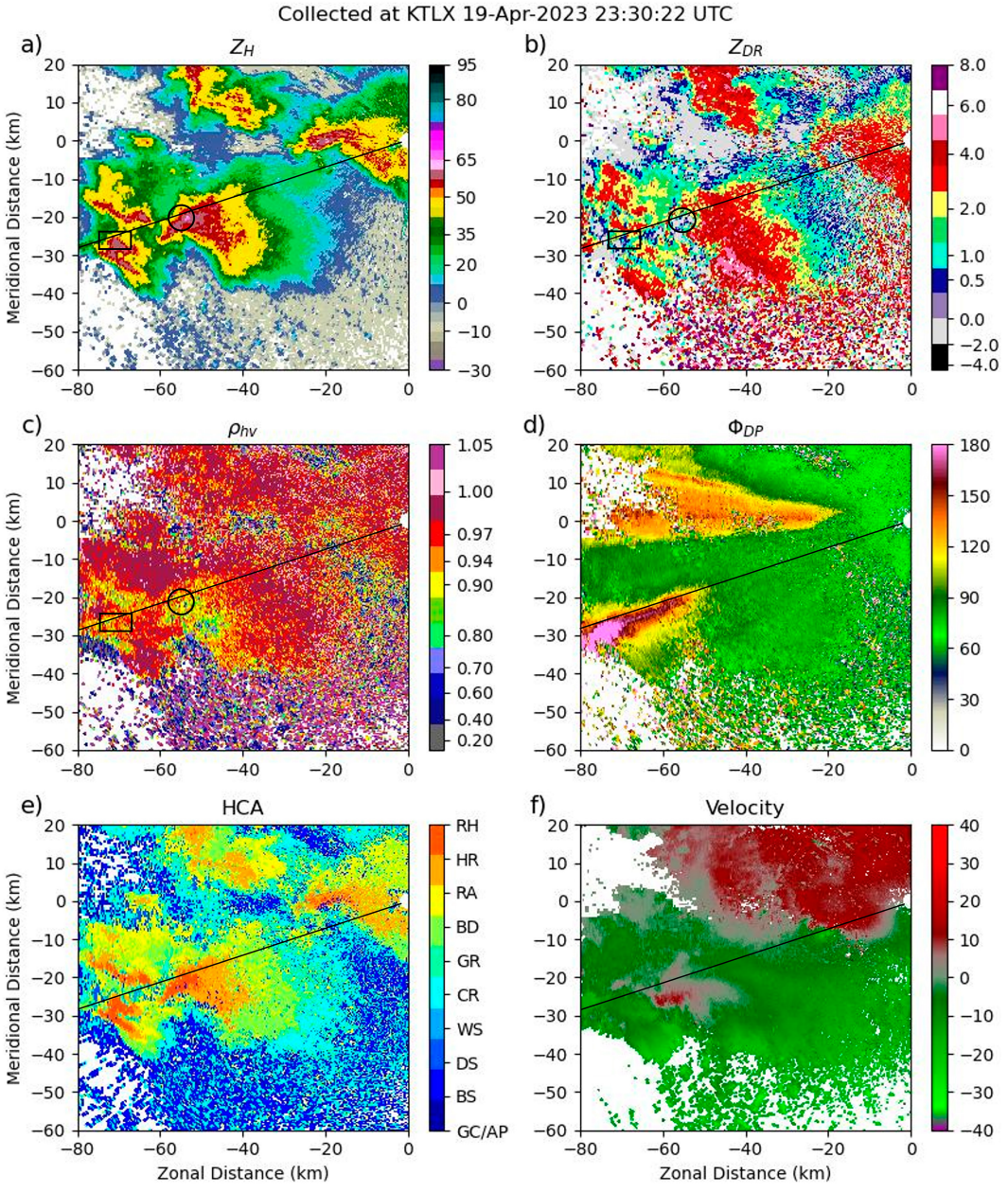

FIG. 5. Low-elevation (0.5°) surveillance mode raw data from KTLX at 2330 UTC. (a) Reflectivity factor Z_H, (b) differential reflectivity Z_{DR}, (c) copolar correlation coefficient ρ_{hv}, (d) total differential phase Φ_{DP}, (e) hydrometeor classification, and (f) radial velocity. The primary region of enhanced reflectivity is denoted with the black circle in (a)–(c), while the second region, farther down radial, is denoted with the black box.

gradients. These tight reflectivity gradients often occur in the presence of significant hail. Due to the broadening of the beam, it could still be capturing hail in one sidelobe, which can reduce ρ_{hv} and affect $\hat{\Phi}_{DP}$. In this nonuniform beamfilling, both Rayleigh and non-Rayleigh scattering occur. The overall reflectivity might be dominated by the lower reflectivity Rayleigh regime due to the higher number concentration, but the presence of large particles in part of the beam resolution can still cause the backscattering phase. Thus, we suspect the presence of δ from non-Rayleigh scatterers to be the key contributors to both bumps in $\hat{\Phi}_{DP}$.

Figure 7 illustrates the 2D results of the new methodology's performance on the Amber, Oklahoma hail case. Figure 7a displays estimated ϕ_{DP}, which captures the broad essence of the measured $\hat{\Phi}_{DP}$ displayed in Fig. 5d with the notable difference being the monotonic increase in values due to estimations only being performed within determined Rayleigh scattering regimes in which, particularly at this low-elevation

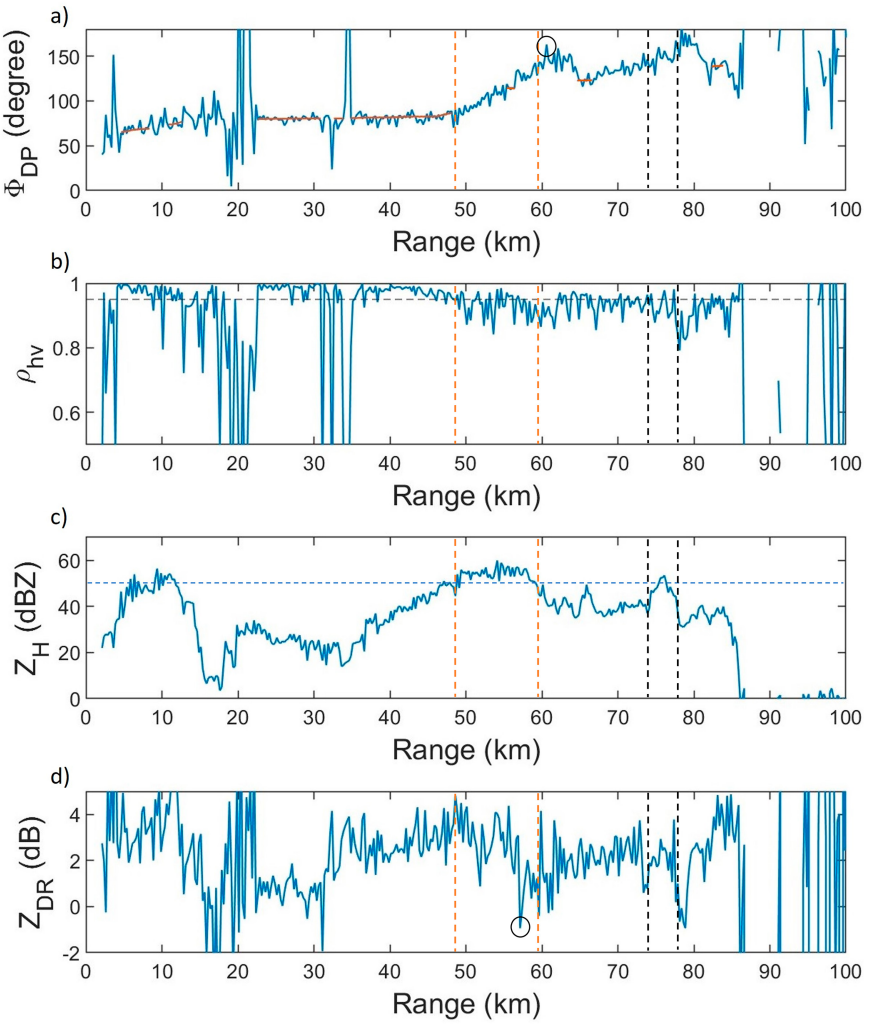

FIG. 6. Ray plots of polarimetric radar data for the highlighted beam in Fig. 5: (a) reflectivity factor Z_H with horizontal black line at 50 dBZ, (b) differential reflectivity Z_{DR}, (c) copolar correlation coefficient ρ_{hv}, and (d) total differential phase Φ_{DP}. The region between the vertical orange dashed lines indicates the first region of enhanced Z_H, while the region between the dashed black lines indicates the second region of enhanced Z_H.

angle (0.5°), the horizontally polarized wave should be more affected than the vertically polarized wave. Taking the difference between the measured $\hat{\Phi}_{DP}$ as seen in Fig. 5d and the estimated ϕ_{DP} displayed in Fig. 7a, we get the estimation of δ which is shown in Fig. 7b. The hail region associated with the defined supercell shows positive δ signatures particularly at the northern and southern peripheries of the core; however, the signature nearly disappears at the core center. This is likely due to the resonance effects illustrated in Fig. 1d.

Figures 7c and 7d illustrate the estimated $\hat{K}_{DP}$ using the LP and the LSF, respectively. The latter shows significantly larger positive values as well as gates with negative $\hat{K}_{DP}$ values. The LSF estimation method applies a range derivative to the measured $\hat{\Phi}_{DP}$, which, as can be seen Fig. 5, can contain well-defined bumps, and results in enhanced $\hat{K}_{DP}$ estimates near the leading edge of the storm followed by negative estimates near the trailing edge, which is evident in Fig. 7d. As can be seen in Fig. 7c, the LP estimation applied only to Rayleigh scattering regimes prevents these issues. This results in significantly reduced $\hat{K}_{DP}$ values and no negative $\hat{K}_{DP}$ in regions that would not make physical sense.

Figure 8 illustrates the 1D plots corresponding to the emphasized ray shown in Figs. 7a–d. Figure 8a plots the estimated ϕ_{DP} (red) against the $\hat{\Phi}_{DP}$ (blue), which helps emphasize the bumps in $\hat{\Phi}_{DP}$ at ~60 km and again at ~78 km from the δ component. The difference between the two plotted lines in Fig. 8a is the estimated δ which is shown in Fig. 8b. Near the range of both hail regimes, we see δ maxima near 50°. The two discussed K_{DP} estimation results are shown together in Fig. 8c. The LSF estimation produces four well-defined bumps in between ~47 and 60 km, which are likely to be artifacts caused by δ and measurement errors. The latter three of these bumps

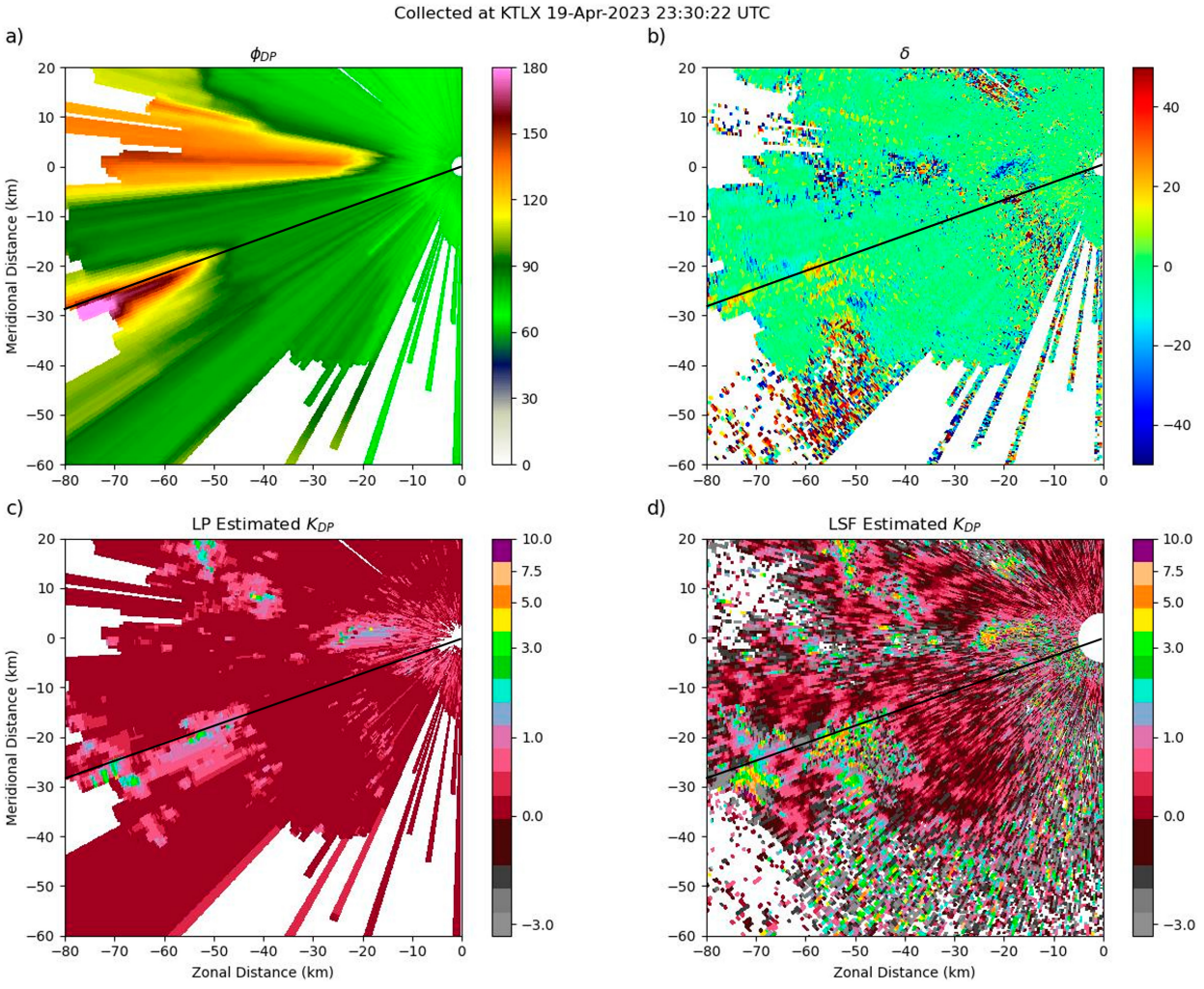

FIG. 7. Estimation results for the image data shown in Fig. 6: (a) estimated differential propagation phase ϕ_{DP}, (b) estimated differential backscattering phase δ, (c) LP estimated K_{DP}, and (d) LSF estimated K_{DP}.

show K_{DP} estimates near 6° km^{-1} with negative values between the peaks. The LP estimation contains the initial $\hat{K}_{DP}$ increase near ~47 km, albeit at a reduced magnitude, though we do not see the trailing spikes seen in the LSF estimate. Instead, we see that the LP estimates remain relatively constant and small before falling slightly near the beginning of the backscattering phase regime near 55 km. We see no jump in the LP $\hat{K}_{DP}$ downrange around the second high reflectivity region. We believe that this is likely due to the lack of Rayleigh scattering regimes between ~65 and 85 km.

An area of enhanced $\hat{K}_{DP}$ within the forward flank of a supercell has acquired the name "KDP foot." Figure 9 presents a zoomed-in view of the primary supercell responsible for 7.6 cm (3 in.) hail reports in Amber, Oklahoma, with the KDP foot signature denoted by the purple line. Figure 9d depicts the LSF $\hat{K}_{DP}$ in which we can see the elevated values particularly along the north-northwestern edge of the supercell where the KDP foot is located. Here, there are multiple gates exceeding 6° km^{-1}. The LP estimation, illustrated in Fig. 9c, shows significantly reduced values of $\hat{K}_{DP}$ across the entire region of the supercell but particularly within the KDP foot region when compared to the LSF results. By restricting the K_{DP} estimation to Rayleigh scattering regions, we minimize the additions of the δ component within the range derivative, which is inherent within the operationally used LSF method. The LP estimation shows a $\hat{K}_{DP}$ maxima in the same location as the maxima in the LSF plot suggesting there is enhanced liquid water content within a portion of the KDP foot signature, but the magnitude of this LP maxima is greatly reduced (~3° km^{-1}), and the enhanced values do not dominate the majority of gates within this region. Figure 9b depicts the estimate of the δ component. We see enhanced values of positive δ along the northwestern and southwestern peripheries of the Z_H maxima. Near the vicinity of the Z_H maxima, we see range gates showing both positive and negative values of δ. We believe that the high variability in δ is likely the result of the non-Rayleigh scattering resonance effects illustrated in Fig. 1d. Furthermore, we see a large negative δ signature

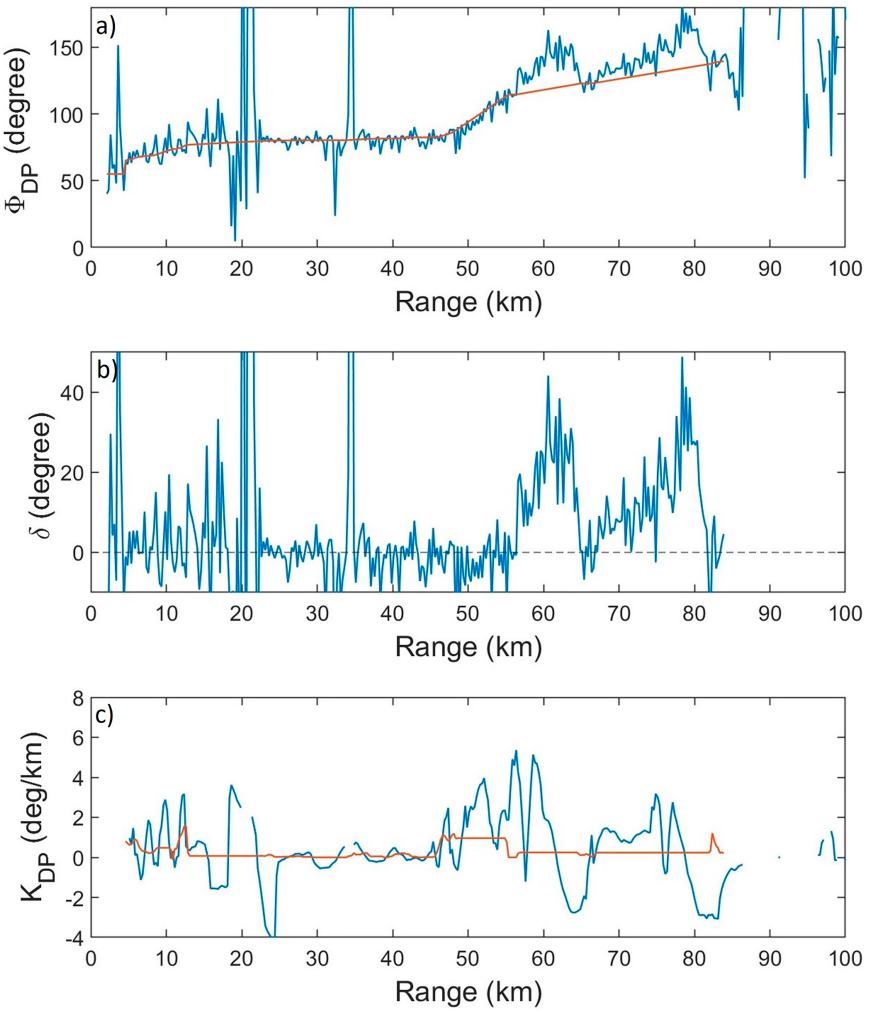

FIG. 8. Estimation results for the highlighted ray plots in Fig. 6: (a) measured total differential phase (blue) and estimated differential propagation phase (red), (b) estimated differential backscattering phase, and (c) LSF estimated K_{DP} (blue) and LP estimated K_{DP} (red).

along the southern edge of the supercell. This is collocated with negative values of $\hat{K}_{DP}$ within the LSF processing plot (Fig. 9d); thus, this is likely the result of the $\hat{\Phi}_{DP}$ drop on the backside of the bump. This results in the estimated ϕ_{DP} being larger than the measured $\hat{\Phi}_{DP}$ for a short range. An example of this can be seen in the 1D plot illustrated Fig. 8a from ~81 to 85 km. The elevated δ values south of the cell (outside of the outlined region) are likely due to low SNR and could be filtered out to improve detection.

With K_{DP} being defined and understood as half the range derivative of the differential propagation phase, in theory, the estimation of K_{DP} should only be valid when restricted to Rayleigh scattering regimes in which the differential backscattering phase is negligible. When that is done, as with the LP K_{DP} estimator, we see a large reduction in the estimated values when compared to the LSF estimator. Thus, the KDP foot, which is characterized by enhanced $\hat{K}_{DP}$ within the forward flank of the supercell, is eliminated. We believe this signature of enhanced values seen within the LSF estimation is due to the range derivative being applied to both the ϕ_{DP} and δ components as opposed to only the propagation phase for which K_{DP} is defined. Hence, the signature commonly referred to as KDP foot is an artifact of flawed methodology utilized within current operational estimations of K_{DP}. Furthermore, as this signature of enhanced values is not actually a result of true K_{DP} (i.e., the range derivative of ϕ_{DP}), we propose that it be retermed as "δ artifact."

The debris lofted into the atmosphere by tornadoes can be larger than or comparable to the wavelength (~10 cm) of an S band radar, yielding radar returns in non-Rayleigh scattering regimes. Hence, we would anticipate TDSs to be associated with noticeable δ signatures. We will look at two separate tornado cases in which well-defined TDSs were present within the radar data.

The evening of 19 April 2023 resulted in severe thunderstorms forming along a dryline in central Oklahoma. One of

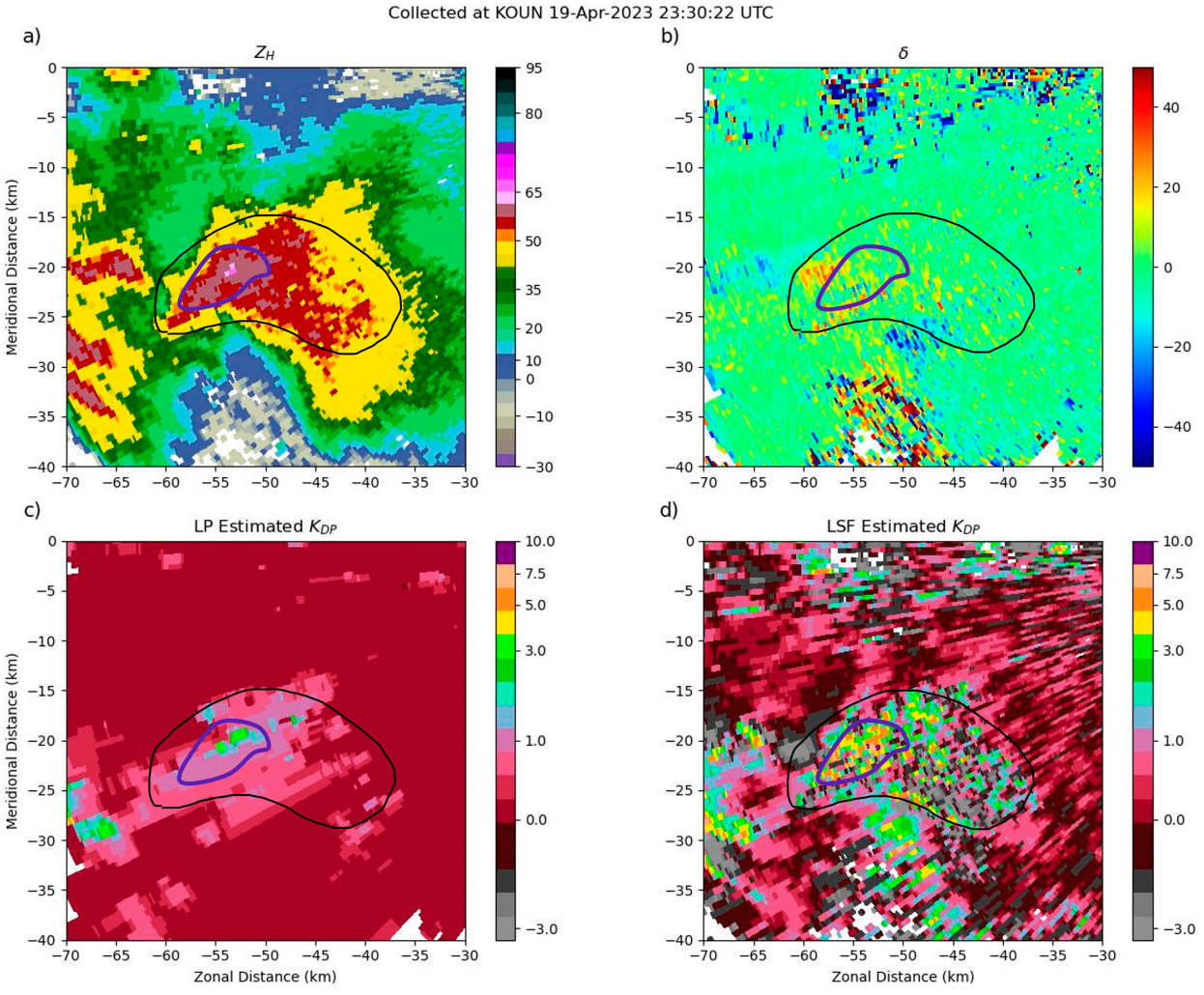

FIG. 9. Primary supercell responsible for reported 3-in. hail in Amber, Oklahoma, corresponding with scans depicted in Figs. 5 and 6. (a) Reflectivity factor Z_H, (b) estimated differential backscattering phase δ, (c) LP estimated K_{DP}, and (d) LSF estimated K_{DP}. The black outline is used to emphasize the area of enhanced K_{DP} seen in the LSF processing. The region of the significantly enhanced values, which is commonly referred to as "KDP foot," is denoted by the region within the purple line.

these storms produced a tornado that struck Cole, Oklahoma, and produced EF3 damage resulting in one fatality (NWS 2023). Below, we analyze the 0035 UTC 20 April 2023 WSR-88D KTLX 0.5° elevation scan file. A black box has been drawn over the top of the TDS on each plot in Fig. 10. Figure 10a depicts the hook echo seen in Z_H descending on the southern side of the supercell where the tornado was located. Figures 10b and 10c help illustrate the TDS with a negative Z_{DR} signature collocated with the ball of low ρ_{hv} (<0.7). As shown in Fig. 1b, the resonance effects caused by large debris can result in highly negative Z_{DR}. Though it is not quite as large as the TDS seen in the ρ_{hv} and Z_{DR} plots, we see a defined, collocated, negative signature of δ in Fig. 10d.

In the evening hours of 24 March 2023, a large tornado ripped through the town of Rolling Fork, Mississippi. This tornado produced EF4 damage and resulted in at least 17 fatalities (NESDIS 2023). We analyze the 0106 UTC 25 March 2023 WSR-88D KGDX (Jackson, Mississippi) 0.5° elevation scan file. Figure 11 depicts the TDS associated with this tornado as it moved into Rolling Fork. We have boxed the region of interest in each of the six plots. Figure 11a shows Z_H values over 60 dBZ embedded within the line at the location of the tornado. Figure 11c depicts a prominent debris signature in the ρ_{hv} data. Similar to the Cole tornado analyzed in Fig. 10, we see ρ_{hv} values fall below 0.7 near the location of the tornado, and Fig. 11b shows us a Z_{DR} signature with values again falling below 0 dB. However, unlike the Cole, Oklahoma, tornado case, we see a predominantly positive δ signature in Fig. 11d. Though a couple of gates near the center of the TDS show negative values of δ ($\sim -20°$), the majority of gates associated with the signature are between 15° and 25°.

Figure 12 presents a side-by-side comparison of the two TDS cases by zooming into the areas boxed in Figs. 10 and 11. Specifically, we focus on the Z_{DR}, ρ_{hv}, and δ signatures. The

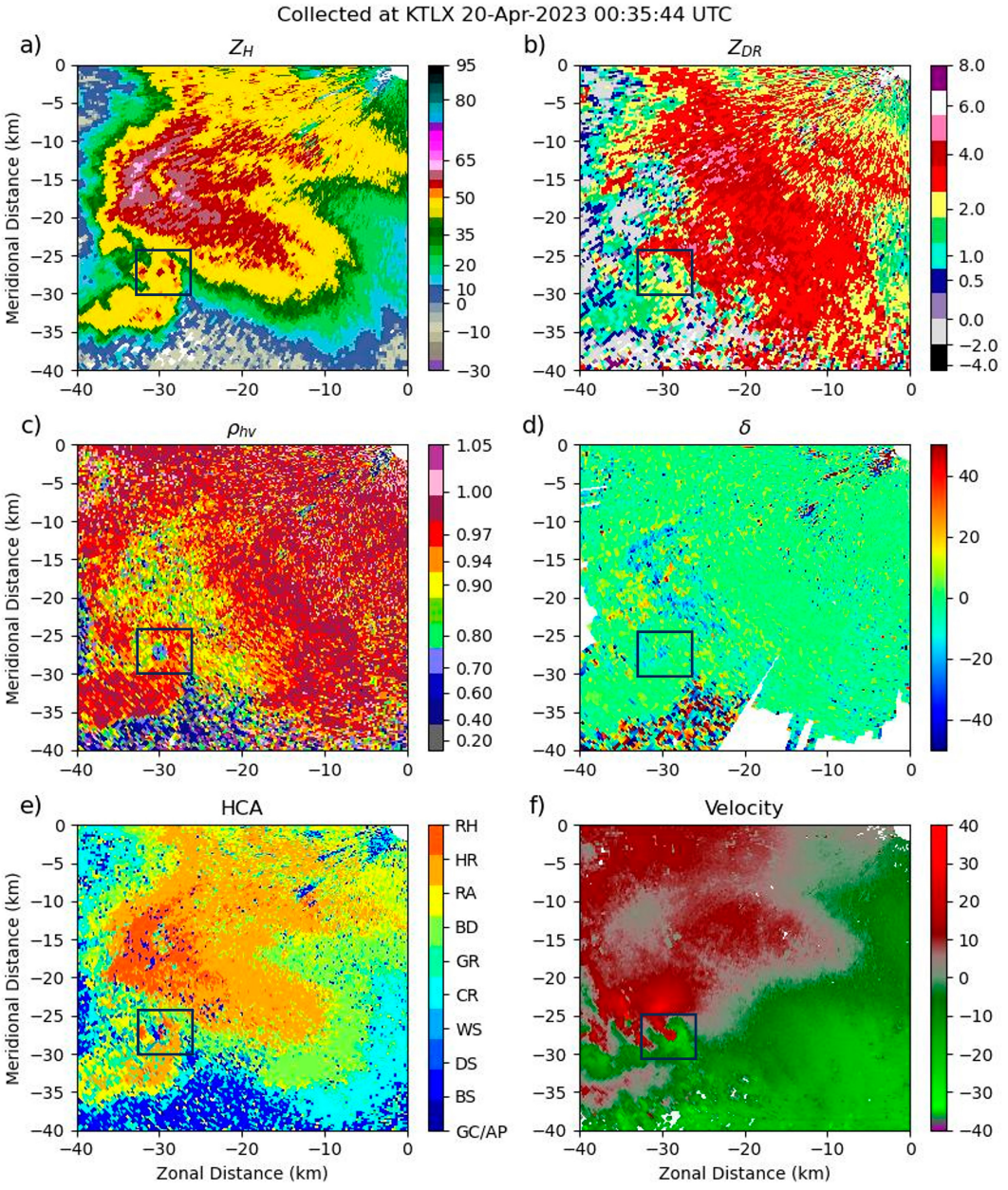

FIG. 10. Low-elevation (0.5°) surveillance mode data from KTLX at 0035 UTC 20 Apr 2023. (a) Reflectivity factor Z_H, (b) differential reflectivity Z_{DR}, (c) copolar correlation coefficient ρ_{hv}, (d) estimated differential backscattering phase δ, (e) hydrometeor classification, and (f) radial velocity. The black box emphasizes the region of the TDS.

difference in the δ signatures between these two tornado cases, seen in Figs. 12c and 12f, could be the result of multiple effects. The Rolling Fork, Mississippi, tornado was much farther away from radar than the Cole, Oklahoma, tornado. Sampling at a farther distance from the radar may result in both precipitation and debris being sampled due to beam broadening. In addition, Fig. 1d illustrates how wet particles display less tendency to produce negative δ than do dry particles. Hence, the positive δ signature might be indicative of a rain-wrapped tornado. This notion is supported by the higher values of ρ_{hv} that surround the TDS in the Rolling Fork, Mississippi, case as compared to that from Cole, Oklahoma, as seen in Figs. 12b and 12f. Finally, as seen in Fig. 1d, the resonance effects associated with scatters outside of the Rayleigh scattering regime can result in positive, negative, and even no δ signature. Though the δ signatures could provide more information regarding the location of these scatterers, the resonance effects may limit the quantitative utilization of δ on its own for the purpose of sizing due to the large variability they cause. However, when it is used together with other

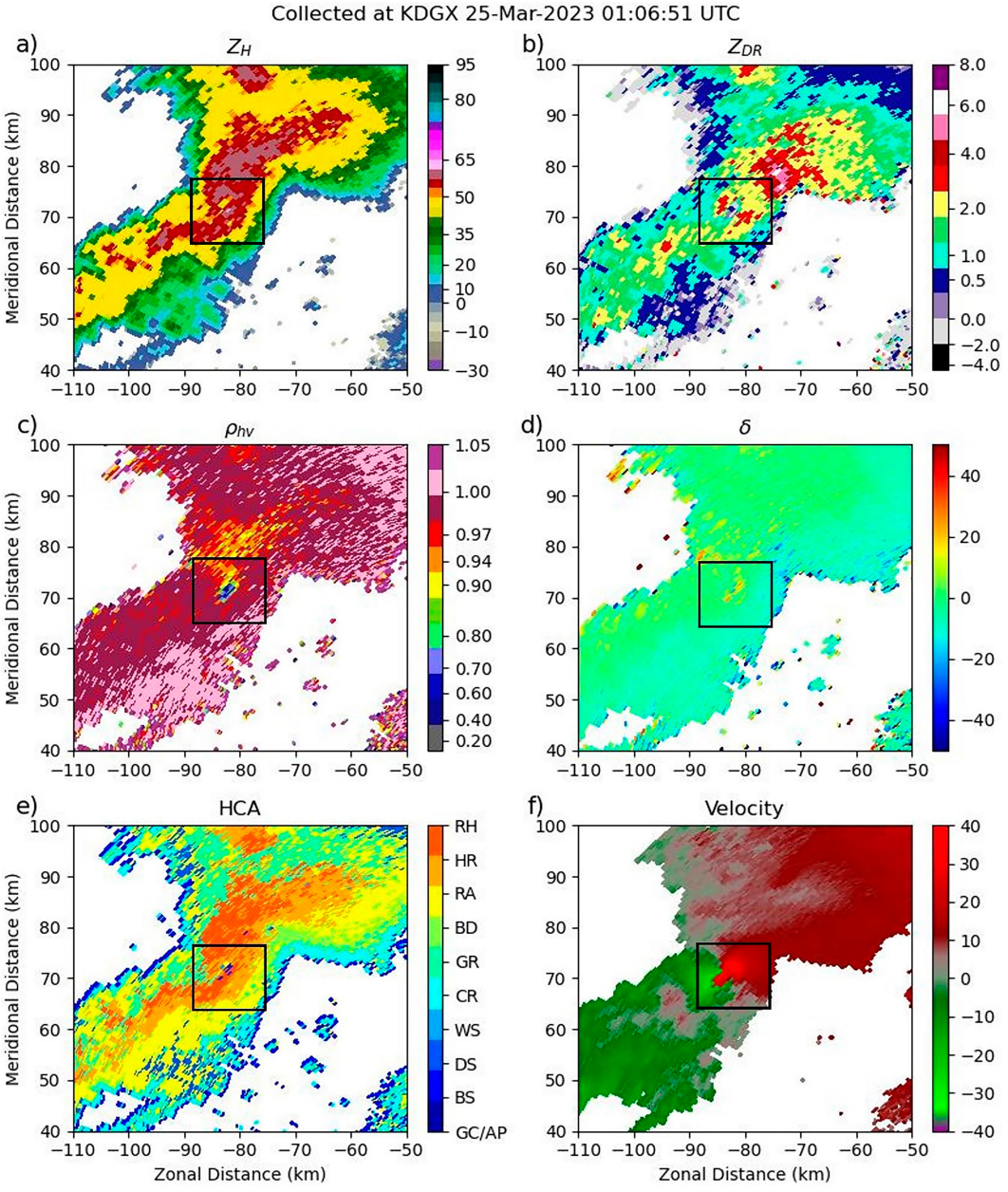

FIG. 11. Low-elevation (0.5°) surveillance mode data from KDGX at 0106 UTC 25 Mar 2023. (a) Reflectivity factor Z_H, (b) differential reflectivity Z_{DR}, (c) copolar correlation coefficient ρ_{hv}, (d) estimated differential backscattering phase δ, (e) hydrometeor classification, and (f) radial velocity. The black box emphasizes the region of the TDS.

polarimetric variables, we speculate δ might still provide helpful information into the size of the scatterer.

5. Summary and conclusions

To explore a more accurate method for K_{DP} estimation, a composite approach of classification and estimation was developed. PRD were classified as Rayleigh and non-Rayleigh scattering regimes, and the LP method was utilized for estimation with built-in nonnegativity constraints. By applying the LP estimation strictly to Rayleigh scattering regimes, we can gather a realistic estimate of the differential propagation phase and eliminate the differential backscattering phase component, which, in the operationally utilized LSF estimation, often leads to unrealistic estimates of K_{DP}. Taking the difference between the measured $\hat{\Phi}_{DP}$ and the estimated ϕ_{DP}, we can estimate δ which looks reasonable and useful.

Scatterers residing outside of the Rayleigh scattering regimes (i.e., hail and tornado debris) display notable δ signatures. However, due to resonance effects with increasingly

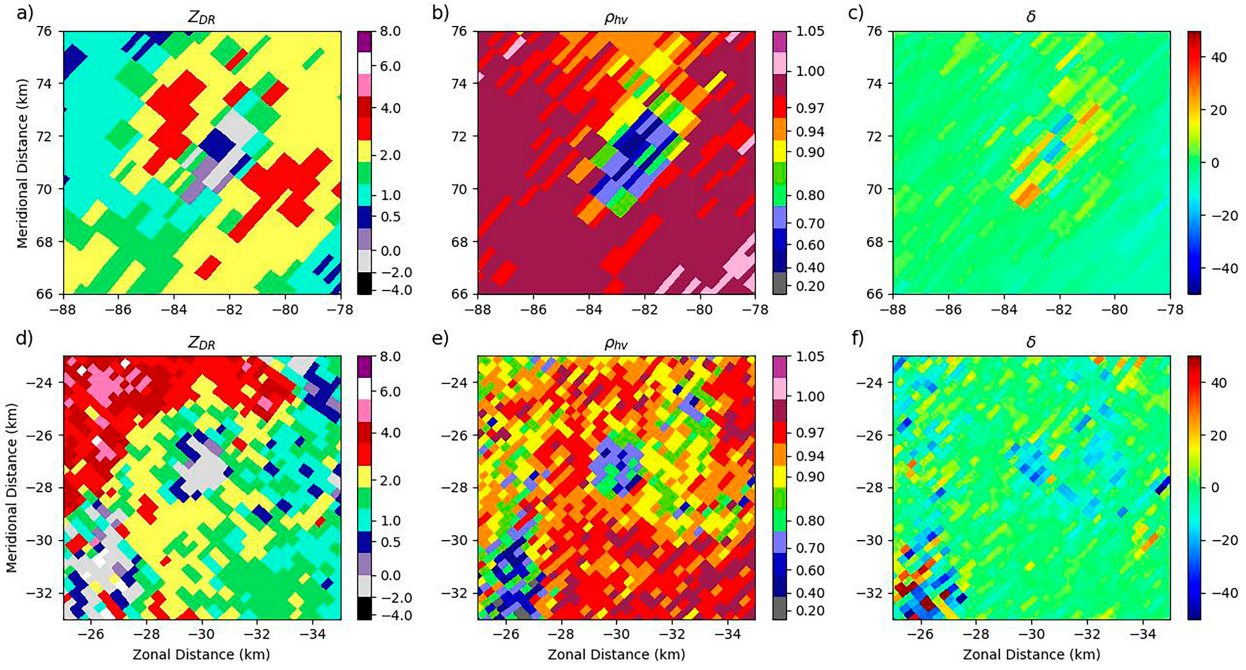

FIG. 12. (a)–(c) 10 km × 10 km views of the Z_{DR}, ρ_{hv}, and δ signatures, respectively, for the Rolling Fork, Mississippi, tornado illustrated in Fig. 11. (d)–(f) As in (a)–(c), but for the Cole, Oklahoma, tornado illustrated in Fig. 10.

larger sizes beyond the Rayleigh scattering regime, these signatures do not appear to display monotonic increases corresponding to increasing Z_H. The analyzed hail case displayed largely positive signatures at the downrange peripheries of the primary hail core, but there is virtually no backscattering phase signature collocated with the gates of maximum Z_H. These resonance effects were further illustrated in the analyzed cases of tornado debris. The EF4 tornado that ravaged Rolling Fork, Mississippi, on 24 March 2023 created a well-defined TDS. The analysis provided a notably positive δ signature collocated with said TDS. However, the EF3 tornado that damaged Cole, Oklahoma, on 19 April 2023, which also produced a well-defined TDS, corresponded with a negative δ signature. These results have shown that while δ can provide helpful information regarding the location of both hail and tornado debris, the resonance effects in both scattering magnitude and backscattering phase complicate the utilization of this product for sizing these scatterers.

The K_{DP} is defined as half of the range derivative of the differential propagation phase. The estimation of this parameter should be limited to Rayleigh scattering regimes exclusively to prevent the error caused by the differential backscattering phase inherent in non-Rayleigh scattering regimes. When comparing the LP $\hat{K}_{DP}$ to the LSF $\hat{K}_{DP}$, we not only see the LP estimates being free of unrealistic negative values, but we also see the LP estimates with significantly reduced magnitudes. Where the LSF estimator might yield values of 6° km^{-1} collocated with the elevated Z_H regions of the supercell, the LP estimator yields values no larger than 3° km^{-1}. The absence of these elevated values in the LP estimation method, which are often seen in the leading side of the supercell with respect to the radar when using the LSF estimation and termed the "KDP foot," emphasizes potential misunderstanding in true K_{DP}. As these elevated estimates (i.e., the KDP foot signature) are only found when the contribution of δ is unaccounted for, the said signature cannot be a result of true K_{DP}. Therefore, we propose that the term KDP foot be retitled as "δ artifact" because of its resulting from the estimation process. This is not to suggest that the LSF estimates are without value at the current stage. The operational community has found use in the interpretation of unphysical estimates, and the technique often provides reasonable results though the uncertainty grows as the scatterer size extends beyond the Rayleigh scattering regime.

There are still many factors and sources of error that have not been fully accounted for and addressed in this work. They include the potential introduction of error when the use of linear interpolation along the non-Rayleigh scattering regimes, the potential presence of clutter, and the possibility of nonuniform beamfilling might potentially introduce error in our estimates and pose limitations to our methodology. Also, though it is relatively rare, propagation cross-polarization coupling, occurring when particle alignments have slantwise orientation, could be a source of error bias for δ. Though there may be some accuracy issues with the estimation along the non-Rayleigh scattering regimes, our primary goal here is to provide a method that would return more reasonable estimates than what is operationally utilized. This study shows the need and feasibility to improve K_{DP} estimation and assess δ for accurate precipitation estimation and severe weather detection. Future studies will aim to enhance and validate the LP estimator through an expanded scope of cases and thorough

error analyses, facilitating its operational implementation and usage.

Acknowledgments. This work was supported by the National Science Foundation with Grant AGS-2136161.

Data availability statement. The NEXRAD Level II data were obtained from Amazon Web Services (https://s3.amazonaws.com/noaa-nexrad-level2).

REFERENCES

AWS, 2023: AWS S3 explorer NOAA NEXRAD Level II. Accessed 21 May 2023, https://s3.amazonaws.com/noaa-nexrad-level2/index.html.

Aydin, K., V. N. Bringi, and L. Liu, 1995: Rain-rate estimation in the presence of hail using S-band specific differential phase and other radar parameters. *J. Appl. Meteor.*, **34**, 404–410, https://doi.org/10.1175/1520-0450-34.2.404.

Balakrishnan, N., and D. S. Zrnić, 1990: Use of polarization to characterize precipitation and discriminate large hail. *J. Atmos. Sci.*, **47**, 1525–1540, https://doi.org/10.1175/1520-0469(1990)047<1525:UOPTCP>2.0.CO;2.

Brandes, E. A., G. Zhang, and J. Vivekanandan, 2002: Experiments in rainfall estimation with a polarimetric radar in a subtropical environment. *J. Appl. Meteor.*, **41**, 674–685, https://doi.org/10.1175/1520-0450(2002)041<0674:EIREWA>2.0.CO;2.

Bringi, V. N., and V. Chandrasekar, 2001: *Polarimetric Doppler Weather Radar: Principles and Applications*. Cambridge University Press, 636 pp.

Doviak, R. J., and D. S. Zrnić, 1993: *Doppler Radar and Weather Observations*. Academic Press, 562 pp.

Giangrande, S. E., and A. V. Ryzhkov, 2008: Estimation of rainfall based on the results of polarimetric echo classification. *J. Appl. Meteor. Climatol.*, **47**, 2445–2462, https://doi.org/10.1175/2008JAMC1753.1.

——, R. McGraw, and L. Lei, 2013: An application of linear programming to polarimetric radar differential phase processing. *J. Atmos. Oceanic Technol.*, **30**, 1716–1729, https://doi.org/10.1175/JTECH-D-12-00147.1.

Huang, H., G. Zhang, K. Zhao, and S. Giangrande, 2016: A hybrid method to estimate specific differential phase and rainfall with linear programming and physics constraints. *IEEE Trans. Geosci. Remote Sens.*, **55**, 96–111, https://doi.org/10.1109/TGRS.2016.2596295.

Jung, Y., G. Zhang, and M. Xue, 2008: Assimilation of simulated polarimetric radar data for a convective storm using the ensemble Kalman filter. Part I: Observation operators for reflectivity and polarimetric variables. *Mon. Wea. Rev.*, **136**, 2228–2245, https://doi.org/10.1175/2007MWR2083.1.

Kumjian, M. R., 2013: Principles and applications of dual-polarization weather radar. Part I: Description of the polarimetric radar variables. *J. Oper. Meteor.*, **1**, 226–242, https://doi.org/10.15191/nwajom.2013.0119.

——, and A. V. Ryzhkov, 2008: Polarimetric signatures in supercell thunderstorms. *J. Appl. Meteor. Climatol.*, **47**, 1940–1961, https://doi.org/10.1175/2007JAMC1874.1.

NESDIS, 2023: Violent storms tear through the South. Accessed 9 October 2023, https://www.nesdis.noaa.gov/news/violent-storms-tear-through-the-south#:~:text=The%20first%20tornadoes%20touched%20down,mph%2C%20that%20injured%20five%20people.

NWS, 2023: The severe weather and tornado outbreak of April 19, 2023. Accessed 9 October 2023, https://www.weather.gov/oun/events-20230419#:~:text=The%20tornado%20that%20occurred%20in,were%20given%20EF%2D0%20ratings.

Otto, T., and H. W. J. Russchenberg, 2011: Estimation of specific differential phase and differential backscatter phase from polarimetric weather radar measurements of rain. *IEEE Geosci. Remote Sens. Lett.*, **8**, 988–992, https://doi.org/10.1109/LGRS.2011.2145354.

Ralph-Hampton, J. M., 2022: Studying the uncertainty in specific differential phase (K_{DP}) from weather radar measurements. Ph.D. dissertation, The University of Leeds, 152 pp., https://etheses.whiterose.ac.uk/31666/1/ralph-hampton_joshua_thesis.pdf.

Rodgers, C. D., 2000: *Inverse Methods for Atmospheric Sounding: Theory and Practice*. World Scientific, 256 pp.

Romine, G. S., D. W. Burgess, and R. B. Wilhelmson, 2008: A dual-polarization-radar-based assessment of the 8 May 2003 Oklahoma City area tornadic supercell. *Mon. Wea. Rev.*, **136**, 2849–2870, https://doi.org/10.1175/2008MWR2330.1.

Ryzhkov, A. V., and D. Zrnić, 1998: Beamwidth effects on the differential phase measurements of rain. *J. Atmos. Oceanic Technol.*, **15**, 624–634, https://doi.org/10.1175/1520-0426(1998)015<0624:BEOTDP>2.0.CO;2.

——, S. E. Giangrande, and T. J. Schuur, 2005a: Rainfall estimation with a polarimetric prototype of WSR-88D. *J. Appl. Meteor.*, **44**, 502–515, https://doi.org/10.1175/JAM2213.1.

——, T. J. Schuur, D. W. Burgess, and D. S. Zrnić, 2005b: Polarimetric tornado detection. *J. Appl. Meteor.*, **44**, 557–570, https://doi.org/10.1175/JAM2235.1.

Seliga, T. A., and V. N. Bringi, 1978: Differential reflectivity and differential phase shift: Applications in radar meteorology. *Radio Sci.*, **13**, 271–275, https://doi.org/10.1029/RS013i002p00271.

SPC, 2023: 20230419's storm reports (20230419 1200 UTC–20230420 1159 UTC). Accessed 16 October 2023, https://www.spc.noaa.gov/exper/archive/event.php?date=20230419.

Trömel, S., M. R. Kumjian, A. V. Ryzhkov, C. Simmer, and M. Diederich, 2013: Backscatter differential phase—Estimation and variability. *J. Appl. Meteor. Climatol.*, **52**, 2529–2548, https://doi.org/10.1175/JAMC-D-13-0124.1.

Vivekanandan, J., W. M. Adams, and V. N. Bringi, 1991: Rigorous approach to polarimetric radar modeling of hydrometeor orientation distributions. *J. Appl. Meteor.*, **30**, 1053–1063, https://doi.org/10.1175/1520-0450(1991)030<1053:RATPRM>2.0.CO;2.

——, G. Zhang, and M. K. Politovich, 2001: An assessment of droplet size and liquid water content derived from dual-wavelength radar measurements to the application of aircraft icing detection. *J. Atmos. Oceanic Technol.*, **18**, 1787–1798, https://doi.org/10.1175/1520-0426(2001)018<1787:AAODSA>2.0.CO;2.

Wang, Y., and V. Chandrasekar, 2009: Algorithm for estimation of the specific differential phase. *J. Atmos. Oceanic Technol.*, **26**, 2565–2578, https://doi.org/10.1175/2009JTECHA1358.1.

——, and ——, 2010: Quantitative precipitation estimation in the CASA X-band dual-polarization radar network. *J. Atmos. Oceanic Technol.*, **27**, 1665–1676, https://doi.org/10.1175/2010JTECHA1419.1.

Waterman, P. C., 1965: Matrix formulation of electromagnetic scattering. *Proc. IEEE*, **53**, 805–812, https://doi.org/10.1109/PROC.1965.4058.

Westbrook, C. D., A. J. Illingworth, E. J. O'Connor, and R. J. Hogan, 2010: Doppler lidar measurements of oriented planar

ice crystals falling from supercooled and glaciated layer clouds. *Quart. J. Roy. Meteor. Soc.*, **136**, 260–276, https://doi.org/10.1002/qj.528.

Wilson, M. B., and M. S. Van Den Broeke, 2021: An automated python algorithm to quantify Z_{DR} arc and K_{DP}–Z_{DR} separation signatures in supercells. *J. Atmos. Oceanic Technol.*, **38**, 371–386, https://doi.org/10.1175/JTECH-D-20-0056.1.

Zhang, G., 2016: *Weather Radar Polarimetry*. CRC Press, 322 pp.

——, J. Gao, and M. Du, 2021: Parameterized forward operators for simulation and assimilation of polarimetric radar data with numerical weather predictions. *Adv. Atmos. Sci.*, **38**, 737–754, https://doi.org/10.1007/s00376-021-0289-6.

Zrnić, D. S., and A. Ryzhkov, 1996: Advantages of rain measurements using specific differential phase. *J. Atmos. Oceanic Technol.*, **13**, 454–464, https://doi.org/10.1175/1520-0426(1996)013<0454:AORMUS>2.0.CO;2.